14th International Symposium on Turbulence and Shear Flow Phenomena (TSFP14)
Heidelberg, Germany, July 28–31, 2026

CHARACTERISATION OF TURBULENT BOUNDARY LAYER INTERFACES SUBJECTED TO FREESTREAM TURBULENCE ASSESSED BY LOCAL INJECTION OF TAGGED PARTICLES IN AIR

Agastya Parikh[1,2], Srikar Yadala[3], Leon Li[3], Rafael Bölsterli[3], Christian J. Kähler[2], & R. Jason Hearst[3]

[1]Department of Fluid Mechanics and Aerodynamics, University of the Bundeswehr Munich,
85577 Neubiberg, Germany
[2]Supersonic and Hypersonic Technologies Department, German Aerospace Center (DLR),
51147 Cologne, Germany
[3]Department of Energy and Process Engineering, Norwegian University of Science and Technology,
Trondheim NO-7491, Norway
agastya.parikh@dlr.de, srikar.y.venkata@ntnu.no

ABSTRACT

Identifying the interface between a turbulent boundary layer (TBL) and a turbulent freestream has posed a considerable challenge which has been tackled with the use of various detection methods. Unlike the turbulent/non-turbulent interface (TNTI), the turbulent/turbulent interface (TTI) lacks a universal defining criterion. The current study approaches this problem with the application of synchronised high-speed Particle Image Velocimetry (PIV) and fluorescent imaging systems to compare interfaces detected via velocity and vorticity thresholds, and tracking of fluorescent particles in a zero-pressure-gradient (ZPG) TBL subjected to varying FST levels. In the canonical TNTI case (low FST level), all three methods yield statistically similar interfaces as expected. However, with increasing turbulence in the freestream, the three interfaces diverge. This is reflected in the probability density functions of interface height, as well as in profiles of streamwise velocity conditioned to instantaneous interface height.

1 INTRODUCTION

The interface of a canonical turbulent boundary layer (TBL) and a laminar freestream above it can be well-identified using a variety of methods; Corrsin & Kistler (1955) defined the Turbulent/Non-Turbulent Interface (TNTI) as the infinitesimally thin shear layer across which the vorticity generated within a turbulent flow is slowly transmitted by viscous action into the irrotational freestream. This naturally led to the conclusion that the corresponding jump in vorticity across the interface could be used as detection criterion. Since then, other criteria such as using local turbulent kinetic energy (Chauhan *et al.*, 2014) or flow homogeneity (Reuther & Kähler, 2018) have been developed. These kinematic methods are used in lieu of a computation of the enstrophy jump through which vorticity is transmitted across the interface due to the lack of readily-available 3D volumetric measurements with sufficient spatial resolution. An alternative strategy working within the limitations of experimental capabilities has been the use of mass tracking, with a passive scalar (Westerweel *et al.*, 2002) or fluorescent particles (Parikh *et al.*, 2025)being employed to segment the flow field into regions containing mass originating within the turbulent flow and the freestream.

The introduction of freestream turbulence (FST) above the boundary layer generally complicates both the definition and identification of instantaneous interfaces (Asadi *et al.*, 2025). In flows with FST, the classical vorticity jump criterion is evidently not applicable, as vorticity exists everywhere in the flow. Other common detection methods such as the TKE (Chauhan *et al.*, 2014) and homogeneity criteria (Reuther & Kähler, 2018) cannot be simply applied experimentally (Hearst *et al.*, 2021). It is also unclear if scalar isocontours can be used as a marker for Turbulent/Turbulent Interface (TTI), given that instantaneously, the vorticity is nonzero in the freestream. The effect of vortex stretching and dissipation is observed on both sides of the TTI (processes not accounted for in the scalar transport equation), which contrasts the results and statements of You & Zaki (2019), Kankanwadi & Buxton (2022) and Asadi *et al.* (2025).

Using the outermost uniform momentum zone (UMZ) to identify the Turbulent/Turbulent Interface (TTI) analogously to the TNTI in canonical flows, Hearst *et al.* (2021) posited that the interfaces yielded mark the boundary between vorticity from the freestream and that generated by the wall. More recently, Asadi *et al.* (2025) separated the FST and the TBL by isolines of momentum and vorticity magnitude by thresholding based on the instantaneous probability density functions of vorticity above and below the isolines. This, in essence, identified that multiple interfaces can hold physical meaning in the case of two turbulent flows interacting, but it remains unclear which one is “the TTI” and if a unique description of the TTI even exists. This contrasts with TNTIs where these interfaces exist in very close proximity instantaneously and are approximately statistically similar.

A universal description of the TTI between a TBL and FST may lie in tracking the mass of the TBL as it evolves beneath FST while also measuring the flow velocity to derive kinematic interfaces for comparison. The present investigation aims to achieve this by applying a flow-tagging approach simultaneously with planar PIV measurements on a ZPG TBL with FST generated using an active turbulence grid. Di-Ethyl-Hexyl-Sebacate (DEHS) doped with Pyrromethene 567, which fluoresces under laser illumination (Okada *et al.*, 2024), acts as an analogue to dye-based passive scalars employed in liquid flows (Westerweel *et al.*, 2002). Local seeding of the

TBL using doped DEHS particles is used to obtain fluorescent particle images, while global seeding of the flow with conventional DEHS particles yields full-field velocimetry (Parikh *et al.*, 2025). This synchronised PIV and fluorescent particle imaging measurement will be used to determine whether the mass interface obtained with this method matches those obtained using kinematic detection criteria.

2 EXPERIMENTAL SETUP

The experiments were conducted in the large-scale recirculating wind tunnel at NTNU, in Trondheim, Norway, which has a cross-section of 1.8×2.7 m^2 and a test section length of 11.1 m. An active turbulence grid, with mesh length of $M = 0.1$ m, was introduced 0.8 m downstream of the contraction to generate highly turbulent freestream conditions (see Li & Hearst, 2025).

A 3.5 m-long flat plate with a sharp leading edge was used to generate the TBL measured during these experiments. The BL plate was installed at a height of 0.65 m above the tunnel's floor. The leading edge was ~ 5.25 m downstream of the active grid, corresponding to $52.5M$, where the incoming flow is approximately homogeneous and isotropic (Yadala *et al.*, 2025). Wall-mounted static pressure taps were used to adjust the plate to achieve $dp/dx \approx 0$ along its length. A 2.5 mm high slot located 0.3 m downstream of the leading edge was used to introduce aerosolised fluorescing DEHS particles to locally seed the boundary layer and simultaneously trip the flow, as in Okada *et al.* (2024). Conventional DEHS droplets produced by a pressurised Laskin-nozzle aerosol generator served as the global seeding.

Measurements were made in a streamwise-wall-normal plane located at the mid-span of the plate and 2.26 m downstream of the trip. Illumination was provided by a single 10 mJ dual-pulse Nd:YAG high-speed laser (Photonics DM 100-532 DH). Two imaging systems working in synchrony at a sampling frequency of 1009 Hz were used to obtain high-speed PIV and fluorescence measurements. Particle image pairs for PIV analysis were captured with a time separation of 100 μs using a Phantom T2540 camera fitted with a Sigma 180 mm lens. A second Phantom T2540 camera was connected to a LaVision HighSpeed IRO intensifier with a Zeiss Milvus 100 mm lens and a 532 nm band-stop filter to isolate the fluorescent emission from the Mie scattering generated by the particles. The PIV field-of-view (FOV) extended up to 0.14 m in the wall-normal direction y, and the fluorescence imaging system was oriented to provide a FOV spanning up to 0.3 m in the wall-normal direction, ensuring capture of the interface even as the TBL thickened under the influence of FST.

A total of three independent time-series, each consisting of ~ 20000 samples, were gathered at each of the four FST levels. However, it is worth noting that in this manuscript, much of the analysis presented is statistical. Therefore, every 25$^{\text{th}}$ field from a single full time-series, corresponding to 823 fields in total, was used to ensure statistical independence between the analysed fields. The final interrogation window size for PIV cross-correlation was 24×24 px^2 with a 50% overlap, yielding a vector spacing of 1.1 mm; the fluorescence images used had a spatial resolution of ~ 0.14 mm.

3 FST AND TBL CHARACTERISTICS

The freestream velocity was maintained at $U_\infty = 8$ m s^{-1} for the different FST conditions tested. The low-turbulence case REF was generated without the active grid. During case A the active grid was installed into the wind tunnel, but it was static and fully open, producing low-intensity turbulence. For cases B and C, approximately homogenous and isotropic turbulent conditions were generated using different "fully random" active-grid sequences, as described by Hearst & Lavoie (2015). The incoming freestream conditions were characterised using hot-wire anemometry (sampled at 75 kHz, analog low-pass filter set to 30 kHz). The probe was situated in the freestream, close to the location where the fluorescing DEHS was injected as it marks the onset of the boundary layer. The resulting turbulence intensity (TI $= \sigma(u_\infty)/\overline{u}_\infty$, where σ represents standard deviation) and integral length scale (L_{uu}) for each case are summarized in Table 1.

The boundary layer characteristics for each case were analysed using the mean velocity fields obtained from planar PIV measurements. A representative profile for each of the boundary layers was obtained by averaging the mean streamwise velocity $\overline{u}$ along the streamwise direction of the FOV. These profiles were fit to log law using a composite profile fit, thereby estimating the friction velocity U_τ. The boundary layer profiles for each case are shown in Fig. 1 in wall coordinates. The boundary layer thickness δ was determined using the iterative integral approach (Perry & Li, 1990) as it is more robust for estimating boundary-layer thickness in the presence of FST (Dogan *et al.*, 2016; Hearst *et al.*, 2021). These parameters, along with the friction Reynolds number $Re_\tau = U_\tau \delta/\nu$, are also reported in Table 1.

A comparison of the different cases reveals an increase in both U_τ and δ with FST, consistent with previous studies (Dogan *et al.*, 2016; Hearst *et al.*, 2021; Asadi *et al.*, 2025). Consequently, Re_τ also increases with incoming FST.

Case	$\sigma(u_\infty)/\overline{u}_\infty$ [%]	L_{uu} [mm]	U_τ [m s^{-1}]	δ [mm]	Re_τ [-]
REF	0.4	-	0.318	59	1261
A	2.2	37	0.327	62	1364
B	6.3	136	0.336	95	2156
C	8.8	166	0.345	107	2489

Table 1: FST and corresponding TBL parameters for $U_\infty = 8$ m s^{-1}. FST statistics were measured close to the TBL onset (where the dye is injected).

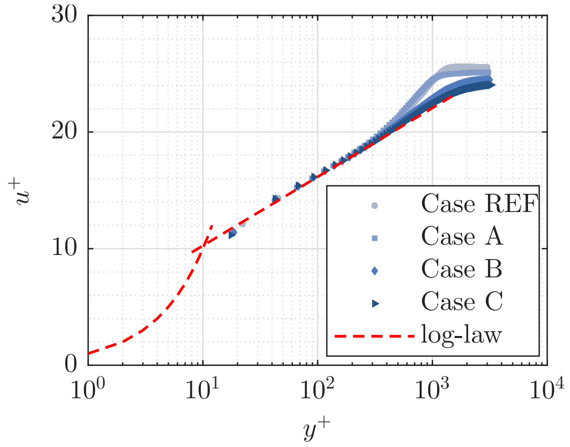

Figure 1: Inner-normalised mean velocity profiles for the different turbulent boundary layers being tested.

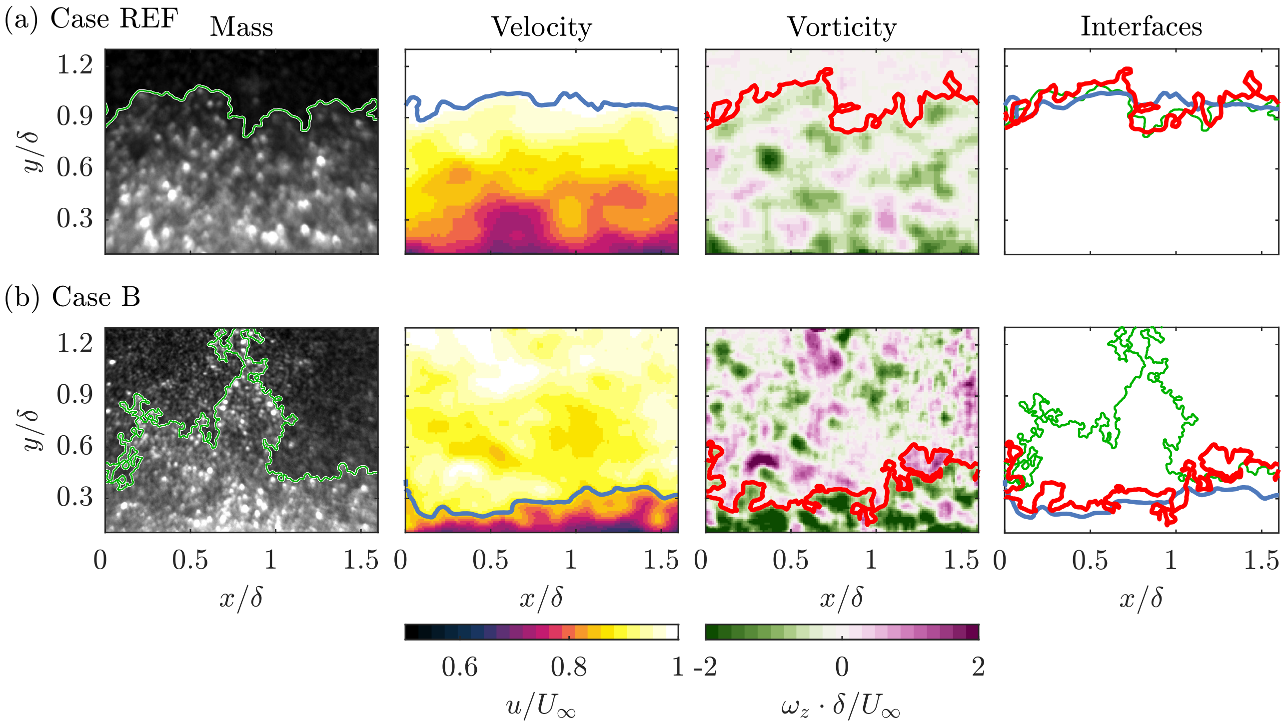

Figure 2: Exemplary TNTI (a, case REF) and TTI (b, case B) detected using, from left to right, fluorescence imaging, and the velocity and vorticity fields at a single time step. Right-most panels show a direct comparison of the three detected interfaces.

4 INSTANTANEOUS INTERFACE DETECTION

Since the focus of this study is the characterisation of interfaces obtained using different methods, a natural initial point of comparison lies in an examination of instantaneous interfaces. Fig. 2(a) illustrates the TNTI from case REF, while Fig. 2(b) depicts the TTI from case B, both representing instantaneous snapshots of the flow from the respective datasets. For each example, three distinct fields are presented, from left to right: the fluorescence images showing tagged DEHS particles, and the streamwise velocity (u/U_∞) and spanwise vorticity ($\omega_z \cdot \delta/U_\infty$) fields obtained from the PIV data at the corresponding instant. Each tile is additionally overlaid with an interface identified using the field shown. The fourth (right-most) tile overlays all three interfaces for a direct comparison.

The mass interface was detected from the fluorescent particle images using a modification of the method of Prasad & Sreenivasan (1989), originally used to detect scalar interfaces in PLIF conducted in a liquid. Morphological image processing consisting of asymmetric closing and eroding operations is first used to convert the particle images into a continuum-like representation of the tagged regions of the flow. The modified fluorescence images are then used to obtain a segmented representation of the FOV. Due to the highly-variable nature of T(N)TIs, which manifests in this case as variations in particle seeding density (and thus apparent intensity) the application of a static intensity threshold to the entire dataset does not delineate the tagged regions of the flow effectively, and an individual threshold is needed. Each image is segmented based on a threshold value I_{th} computed from a function representing the average intensity of the image $\langle I \rangle$ evaluated over all pixels with an intensity $I > I_{th}$. The zero crossing of the Laplacian of this function yields I_{th} based on the characteristics of the image. Subsequently, the interface delineating tagged mass is trivially identified using edge-detection algorithms. A more detailed description and further validation of the detection method can be found in Parikh *et al.* (2025).

The velocity and vorticity interfaces were detected using the method proposed by Asadi *et al.* (2025). This approach identifies interfaces by comparing the vorticity distribution on either side of continuous isolines of velocity or vorticity. Two key conditions must be satisfied for an isoline to qualify as an interface. First, the Euclidean distance D between the probability density functions (p.d.fs) of vorticity on the boundary-layer side and the freestream side of an isoline must exceed a threshold value D_{th}, ensuring a statistically significant distinction between the two regions. Second, the median M of the vorticity distribution on the boundary-layer side of the isoline must be smaller than a negative threshold ($M < M_{th}$), which reflects the effect of the wall and the mean shear. For the first condition, the vorticity distribution in the freestream was analysed using the seven top-most rows of vectors in the PIV field. The Euclidean distance between instantaneous and mean p.d.fs ensemble-averaged over all the considered vector fields, $D_{i,FST}$, was computed. For the second condition, the median vorticity, $M_{i,FST}$, above the top-most continuous isoline was determined for each instantaneous field. For the current data, threshold values of $D_{th} = \sigma(D_{i,FST})$ and $M_{th} = \sigma(M_{i,FST})$ (σ representing standard deviation) distinguished the boundary layer vorticity distribution from oscillations in the freestream fairly well.

The right-most tile of Fig. 2(a) overlays all three interfaces for direct comparison. The velocity interface appears as a smooth line, while the mass and vorticity interfaces exhibit finer-scale features that contribute to localized discrepancies. The smaller features visible in the mass interface are a result of the higher spatial resolution of a non-windowed detection method, while for the vorticity interface, some of the smaller features may be attributed to noise associated with the compu-

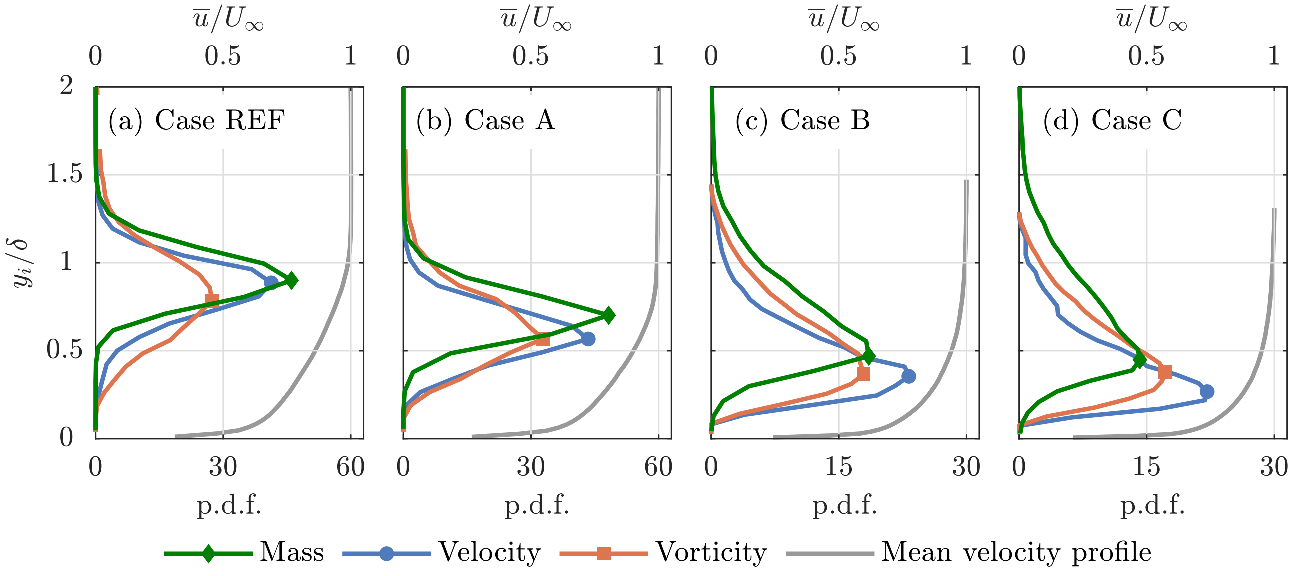

Figure 3: P.d.fs of the instantaneous interface location y_i/δ obtained from velocity and vorticity fields, and fluorescent particle images for the four test cases. The corresponding mean velocity profile is also shown.

tation of gradients. Nevertheless, the three interfaces do converge to a similar wall-normal height. This observation is consistent with the canonical understanding of TNTIs, where the lack of any vorticity/turbulent fluctuations in the freestream means that all interfaces should roughly align with one another.

Exemplary TTIs detected using the three methods in case B are presented in Fig. 2(b). In contrast to case REF, where the interface between the TBL and the freestream is easily discernible in all three fields, the presence of FST in case B complicates the identification of a clear interface. Both the vorticity and tagged particles are no longer confined to just the boundary layer and appear to be distributed over the FOV. For the velocity and vorticity interfaces, the employed detection method dynamically adapts to the presence of FST and is robust enough to handle such scenarios requiring dynamic thresholding as demonstrated by Asadi *et al.* (2025). Focusing on the right-most tile in Fig. 2(b) where the three interfaces are juxtaposed, the velocity interface (blue) remains relatively smooth, while the mass (green) and vorticity (red) interfaces exhibit finer-scale features, as observed with case REF. However, the most striking observation is the disparity in the wall-normal location of the mass interface compared to the velocity and vorticity interfaces. This divergence underscores the complexity of defining TTIs in the presence of FST, where tagged mass, velocity, and vorticity may capture distinct interfaces.

5 INTERFACE STATISTICS

To statistically investigate the behaviour observed in the instantaneous interfaces—particularly under FST—the p.d.fs of the wall-normal locations of the various interfaces y_i are presented in Fig. 3 and the mean interface height $\overline{y}_i$ is shown in Fig. 4. Along the with the p.d.fs of the mass, velocity, and vorticity interfaces, the mean velocity profile of the respective boundary layers is also plotted in Fig. 3 for reference. For the low-turbulence case REF (Fig. 3(a)), the p.d.fs of the three interfaces exhibit Gaussian-like profiles. As expected for a canonical TNTI, the distributions of the velocity and mass interfaces align closely. Although the p.d.f of the vorticity interface is broader and shallower, the wall-normal location of

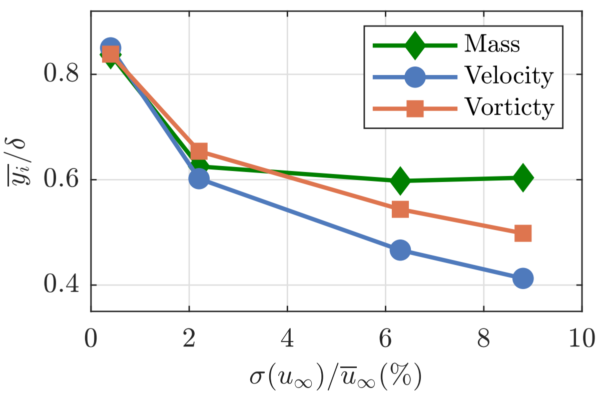

Figure 4: Mean interface height with varying FST intensity.

its peak and the mean TNTI height align well with those of the other two interfaces. Furthermore, the height of the TNTIs are lower than the boundary layer thickness here, which is in agreement with Chauhan *et al.* (2014). These observations provide good confirmation of the statistical similarity of the interfaces in the absence of FST.

The introduction of FST fundamentally alters the statistical behaviour of the interface, as starkly illustrated by the p.d.fs of the interface height in Fig.3(b-d). With increasing FST intensity, the p.d.fs develop a pronounced skewness in line with previous studies (You & Zaki, 2019; Asadi *et al.*, 2025). While the wall-normal location of their maxima tends towards the wall, their tails extend farther into the freestream with increasing FST. This dual trend reflects two key observations. First, the downward shift of the p.d.f maximum along with the same trend in $\overline{y}_i$ demonstrates the interfaces' increasing likelihood to be found closer to the wall. This is analogous to the observation of Hearst *et al.* (2021), who demonstrated that the uppermost UMZ edge is pushed toward the wall with increasing FST. Second, the long tails of these p.d.f. distributions into the freestream are indicative of the interfaces undergoing larger excursions into the freestream with increasing FST. The velocity and vorticity interfaces following these

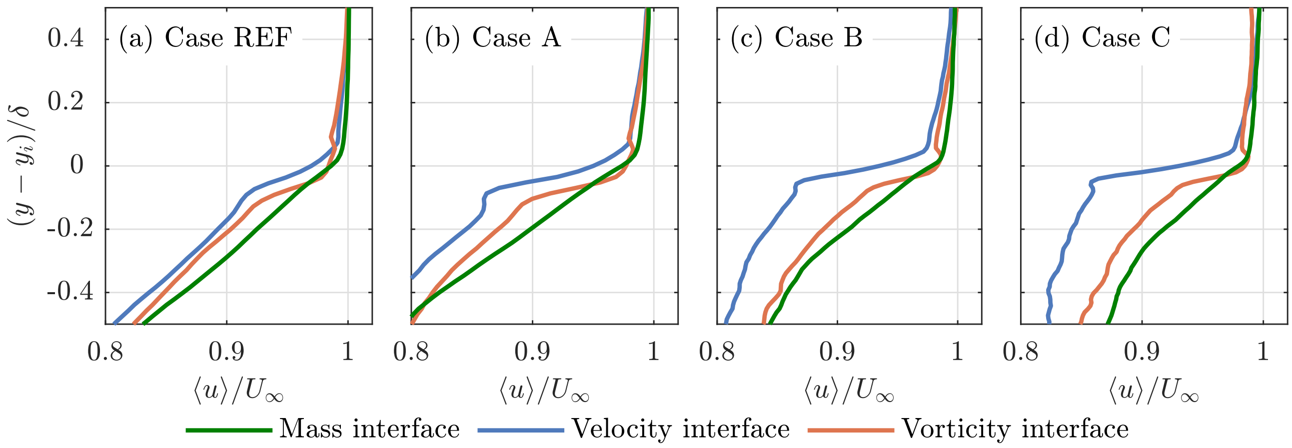

Figure 5: Profiles of $\langle u \rangle / U_\infty$, conditioned to the mass, velocity, and vorticity interfaces for each of the four test cases.

trends is in agreement with Asadi *et al.* (2025). It is noteworthy that the interface obtained from fluorescence imaging, despite tracking the boundary-layer mass rather than any kinematic quantities, also follows these trends, thereby demonstrating the universal impact of FST on TTI behaviour.

The comparison of interfaces' wall-normal locations reveals that the alignment between mass tracking-, velocity-, and vorticity-based methods weakens with increasing FST, which is in line with the observation made when comparing the instantaneous interfaces of case B earlier in Fig. 2(b). Specifically, the p.d.f.-maxima of the velocity and vorticity interfaces continue to move downward with increasing FST. This trend is more apparent with $\bar{y}_i$ in Fig. 4 where the mean wall-normal location of these two interfaces linearly decrease with FST. Contrarily, while the mass maximum of the mass interface p.d.f exhibits the same downward shift, the mean interface location stagnates near $y/\delta \approx 0.6$.

6 CONDITIONAL VELOCITY PROFILES

To extend the analysis and determine whether there is a physical meaning behind the variation in the behaviour of the different interfaces, profiles of mean streamwise velocity conditioned on the instantaneous interface height (y_i) were extracted from the PIV dataset. To account for the possibility of a multivalued interface height caused by the contour curling back on itself, the highest interface position at a given streamwise location was chosen to generate an "outer" envelope with which to condition the flow field.

Fig. 5 depicts conditioned profiles of $\langle u \rangle / U_\infty$, plotted in the interface coordinate $(y - y_i)/\delta$. Similar to the interfacial statistics, all three interfaces show relatively good agreement for cases REF and A, where the TBL is near-canonical and the influence of FST is minimal. However, increasing FST again shows an increase in disparity between the conditional profiles obtained with different methods. For case B, the velocity interface tends more clearly towards a sharp velocity gradient immediately below the interface, while the vorticity and mass interfaces show better agreement and a shallower gradient. For case C, while the profiles conditioned with the vorticity and mass interfaces lie closer than that conditioned to the velocity interface, the disparity between them continues to increase. This behaviour is reflected in the p.d.fs of the instantaneous interface locations in Fig. 3; as FST increases, the p.d.fs are increasingly skewed towards the wall, and stronger gradients in the wall-normal direction are expected.

The extraction of mean velocity profiles conditioned to interface height, shown for cases REF and B in Fig. 6, highlights these differences further. The height-based profiles for case REF, in Fig. 6(a), show good agreement between the different interfaces. However, the profiles conditioned to the velocity interface exhibit a more prominent gradient in the immediate vicinity of the interface for $y_i/\delta > 1$. This behaviour is more starkly illustrated in Fig. 6(b), where significant FST is introduced. Here, the profiles conditioned to the mass and vorticity interfaces are more limited in their agreement and only retain similarity for $y_i/\delta < 1$, and the apparent wall-normal gradient in u around the interface is far more pronounced for the profiles conditioned to velocity interfaces. Notably, the conditional profiles for all interfaces are increasingly disparate at large instantaneous interface heights and bear little similarity to each other.

7 SUMMARY AND OUTLOOK

Unlike for canonical TBLs, the instantaneous edge of the boundary layer in the presence of turbulence in the freestream is poorly-defined. To better understand the physical characteristics of the interfaces generated using different detection methods, a TBL subjected to varying levels of FST was observed using synchronised PIV and fluorescent imaging. Fluorescing DEHS particles were used to tag mass associated with the TBL and extract interfaces based on the method described in Parikh *et al.* (2025). Velocity and vorticity interface detection schemes based on the work of Asadi *et al.* (2025) were applied to obtain interfaces rooted in velocimetry.

A statistical comparison of the interfaces obtained shows that all methods exhibit good agreement in p.d.fs of instantaneous interface location as well as in flow statistics conditioned to the interface where little to no FST is present. However, as FST increases, the disparity between the interfaces detected does as well; the velocity interfaces skew closer to the wall, while the mass interfaces tend to be higher. The vorticity interfaces generally lie between the two. This behaviour is mirrored in profiles of streamwise velocity conditioned to the different interfaces. Profiles conditioned to instantaneous interface height indicate that the disparity observed is also a function of distance from the wall, with interfaces far away from the wall yielding markedly different velocity profiles. These results demonstrate that the impact of FST on TBL behaviour is universal and independent of the interface being used to define it.

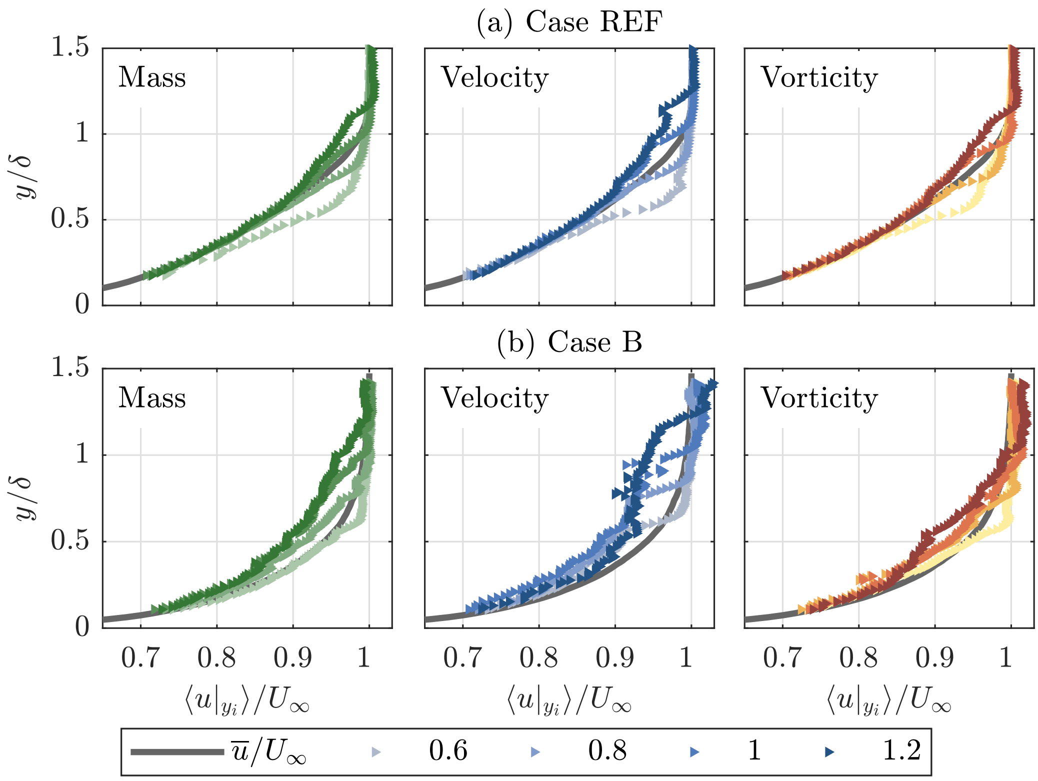

Figure 6: Profiles of $\langle u|_{y_i}\rangle/U_\infty$, conditioned to various interface heights for (a) case REF and (b) case B.

ACKNOWLEDGEMENTS

This research is partly funded by the European Union (ERC StG 101041000, GLITR). Views and opinions expressed are, however, those of the authors only and do not necessarily reflect those of the European Union or the European Research Council. Neither the European Union nor the granting authority can be held responsible for them.

REFERENCES

Asadi, M., Bullee, P.A. & Hearst, R.J. 2025 The instantaneous structure of a turbulent wall-bounded flow influenced by freestream turbulence: streamwise evolution. *J. Fluid Mech.* **1005**, A2.

Chauhan, K., Philip, J., de Silva, C.M., Hutchins, N. & Marusic, I. 2014 The turbulent/non-turbulent interface and entrainment in a boundary layer. *J. Fluid Mech.* **742**, 119–151.

Corrsin, S. & Kistler, A.L. 1955 Free-Stream Boundaries of Turbulent Flows. NACA technical report 1244. NACA.

Dogan, E., Hanson, R.E. & Ganapathisubramani, B. 2016 Interactions of large-scale free-stream turbulence with turbulent boundary layers. *J. Fluid Mech.* **802**, 79–107.

Hearst, R.J. & Lavoie, P. 2015 The effect of active grid initial conditions on high Reynolds number turbulence. *Exp. Fluids* **56** (185).

Hearst, R.J., de Silva, C.M., Dogan, E. & Ganapathisubramani, B. 2021 Uniform-momentum zones in a turbulent boundary layer subjected to freestream turbulence. *J. Fluid Mech.* **915**, A109.

Kankanwadi, K.S. & Buxton, O.R.H. 2022 On the physical nature of the turbulent/turbulent interface. *J. Fluid Mech.* **942**, A31.

Li, L. & Hearst, R.J. 2025 Effects of freestream turbulence on the wakes of circular and square cylinders. *Phy. Rev. Fluids* **10** (11), 114610.

Okada, M., Parikh, A., Pinho, J., Kähler, C.J. & Lavagnoli, S. 2024 A fluorescent particle for PIV in gas phase flows. *Exp. Fluids* **65** (10).

Parikh, A., Okada, M., Bertelli, F., Lavagnoli, S. & Kähler, C.J. 2025 Analysis of turbulent flows by simultaneous fluorescent and Mie-scattering PIV. *Exp. Fluids* **66** (3).

Perry, A.E. & Li, J.D. 1990 Experimental support for the attached-eddy hypothesis in zero-pressure-gradient turbulent boundary layers. *J. Fluid Mech.* **218**, 405–438.

Prasad, R.R. & Sreenivasan, K.R. 1989 Scalar interfaces in digital images of turbulent flows. *Experiments in Fluids* **7**, 259–264.

Reuther, N. & Kähler, C.J. 2018 Evaluation of large-scale turbulent/non-turbulent interface detection methods for wall-bounded flows. *Exp. Fluids* **59**.

Westerweel, J., Hofmann, T., Fukishima, C. & Hunt, J.C.R. 2002 The turbulent/non-turbulent interface at the outer boundary of a self-similar turbulent jet. *Exp. Fluids* **33**, 873–878.

Yadala, S., Dehareng, S., Neunaber, I., Jankee, G.K., Kaufmann, R., Couliou, M. & Hearst, R.J. 2025 The effect of turbulence on a flexible finite wing: forces, deflections and the wingtip vortex. *J. Fluid Mech.* **1019**, A38.

You, J. & Zaki, T.A. 2019 Conditional statistics and flow structures in turbulent boundary layers buffeted by free-stream disturbances. *J. Fluid Mech.* **866**, 526–566.